Song *et al.*
Chinese Journal of Mechanical Engineering (2023) 36:83
https://doi.org/10.1186/s10033-023-00909-2

Chinese Journal of Mechanical Engineering

ORIGINAL ARTICLE

Open Access

Three-Dimensional Conjugate Tooth Surface Design and Contact Analysis of Harmonic Drive with Double-Circular-Arc Tooth Profile

Chaosheng Song[1*], Feihong Zhu[1], Xinzi Li[1] and Xuesong Du[1]

Abstract

A three-dimensional conjugate tooth surface design method for Harmonic Drive with a double-circular-arc tooth profile is proposed. The radial deformation function of the flexspline (FS), obtained through Finite Element (FE) analysis, is incorporated into the kinematics model. By analyzing the FS tooth enveloping process, the optimization of the overlapping conjugate tooth profile is achieved. By utilizing the hobbing process, the three-dimensional machinable tooth surface of FS can be acquired. Utilizing the coning deformation of the FS, simulations are conducted to analyze the multi-section assembly and meshing motion of the machinable tooth surface. The FE method is utilized to analyze and compare the loaded contact characteristics. Results demonstrate that the proposed design method can achieve an internal gear pair consisting of a circular spline with a spur gear tooth surface and the FS with a machinable tooth surface. With the rated torque, approximately 24% of the FS teeth are engaged in meshing, and more than 4/5 of the tooth surface in the axial direction carries the load. The contact patterns, maximum contact pressure, and transmission error of the machinable tooth surface are 227.2%, 40.67%, and 71.24% of those on the spur gear tooth surface, respectively. It clearly demonstrates exceptional transmission performance.

Keywords Three-dimensional conjugate tooth surface, Coning deformation, Double-circular-arc tooth profile, Harmonic Drive, Contact characteristics

1 Introduction

The Harmonic Drive (HD) consists mainly of three components: the flexspline (FS), circular spline (CS), and wave generator (WG). It is widely utilized in aerospace, industrial robotics, and other fields due to its compact structure, high transmission ratio, and precise transmission capabilities. However, the FS exhibits spatial features, particularly in the case of short-cup FS, due to its elastic coning deformation. To achieve optimal contact characteristics, it is essential to design the tooth surfaces of both the FS and CS as spatially conjugate surfaces. Therefore, establishing an HD kinematics model based on the coning deformation of the FS and designing a three-dimensional (3D) conjugate tooth surface for the FS hold critical significance.

Many researchers have carried out a lot of work in the field of HD structure design [1, 2], meshing theory [3–5], tooth profile design [5–9], backlash and meshing force distribution [10]. In terms of the design of HD conjugate tooth profile, Yang et al. [11] proposed an exact solution for two-dimensional (2D) conjugate profiles of zero-backlash HDs with elliptical cam WG. Dong et al. [1, 4] proposed an HD kinematics model considering the deformation of FS. They emphasized that in order to avoid unnecessary interference and deformation, one of the tooth surfaces of FS and CS must be a spatial tooth surface. Wu et al. [12] proposed that the tooth surface of CS adopts the spatial tooth surface, and that of the FS

*Correspondence:
Chaosheng Song
chaoshengsong@cqu.edu.cn
[1] State Key Laboratory of Mechanical Transmissions, Chongqing University, Chongqing 400030, China

Springer Open

© The Author(s) 2023. **Open Access** This article is licensed under a Creative Commons Attribution 4.0 International License, which permits use, sharing, adaptation, distribution and reproduction in any medium or format, as long as you give appropriate credit to the original author(s) and the source, provide a link to the Creative Commons licence, and indicate if changes were made. The images or other third party material in this article are included in the article's Creative Commons licence, unless indicated otherwise in a credit line to the material. If material is not included in the article's Creative Commons licence and your intended use is not permitted by statutory regulation or exceeds the permitted use, you will need to obtain permission directly from the copyright holder. To view a copy of this licence, visit http://creativecommons.org/licenses/by/4.0/.

adopts the spur gear tooth surface. However, it is difficult to achieve mass production of CS spatial tooth surfaces. Considering the coning deformation of FS, Liu et al. [13] converted the design of the 3D tooth surface of CS into a 2D tooth profile design in multiple cross-sections. Wang et al. [14] discretized the FS tooth surface into many cross-sections normal to the rotating axis, and designed the FS tooth surface by reasonably adjusting the position of the FS tooth profile along the radius. Chen et al. [15] analyzed the spatial coning deformation features of the FS based on the straight generatrix assumption. In view of the problem that there is a certain deviation between the actual deformation and the assumed linear deformation, Li et al. [16] uses the finite element method to explore the influence of the structural parameters on the radial deformation of FS. The tooth surface of the FS is modified based on the simulation results of the FS deformation. Papers cited above treat the tooth surface of the harmonic gear as a series of discrete cross-sectional tooth profiles for designing the conjugate tooth surface. Some researchers have taken into account the impact of the FS coning deformation on the design of the tooth surface of harmonic gears. However, they have not thoroughly analyzed the coning deformation of the FS, resulting in qualitative conclusions instead of quantitative results. Hence, it is crucial to consider the manufacturing technology of both the FS and the CS, conduct a detailed analysis of the coning deformation of the FS, and develop a 3D tooth surface design method that aligns more closely with practical engineering requirements.

This paper presents a novel method for designing a 3D conjugate tooth surface with a double-circular-arc tooth profile in HD. The approach incorporates the radial deformation function of the FS obtained through FEA into the kinematics model of HD. By considering the hobbing process of FS, the position of the main section tooth profile along the radial direction is adjusted to achieve the 3D conjugate tooth surface of FS. Additionally, accounting for the coning deformation of FS, a multi-section assembly and meshing motion simulation of the 3D conjugate tooth surface are performed. Finally, the loaded contact characteristics of the FS are analyzed and compared using the finite element method, both with the spur gear tooth surface and the 3D conjugate tooth surface.

2 Kinematics Model of Harmonic Drive Considering the Coning Deformation of FS

If the combined effect of complex factors such as the actual geometry of the flexible bearing and the transition fillet of the gear ring is considered, the kinematics of HD will be very complicated. Therefore, to simplify the problem, the following assumptions are made.

(1) The displacement of the FS along the rotating axis direction is negligible [7].
(2) There is a curved surface inside the thin-wall cylinder of the FS that cannot be elongated, which is called the FS neutral surface.
(3) The elastic deformation state of the FS neutral surface is stable, ignoring the slight swing relative to the average position caused by the distribution of meshing gear teeth.
(4) The intersected curve between the FS neutral surface and each cross-section normal to the rotating axis is the neutral curve in this section. The neutral curve in each section is not elongated and is a standard ellipse with different eccentricities.
(5) The FS is manufactured in an undeformed state, and the FS teeth are regarded as rigid bodies connected by a flexible ring.

As shown in Figure 1, the coning deformation of the FS is considered to establish an HD coordinate system. The CS is fixed, the WG is the input, and the FS is the output. The coordinate system $S(O\text{-}XYZ)$ is fixedly connected to the WG, the Z-axis coincides with the rotating axis, and the X-axis is the major axis of the WG. The coordinate system $S_1(O_1\text{-}X_1Y_1Z_1)$ is fixedly connected to the FS tooth, the X_1 axis is the symmetrical line of the FS tooth profile, and the origin O_1 is the intersected point of the X_1 axis and the FS neutral curve. The coordinate system $S_2(O_2\text{-}X_2Y_2Z_2)$ is connected to the CS, and the Z-axis also coincides with the rotating axis. At the initial position, the coordinate system S and S_2 coincide, the origin O_1 is located at the vertex of the WG major axis, and the 3 axes X_1, X_2 and X are collinear. The WG rotates counterclockwise by angle ϕ_2 relative to the X_2 axis, the designated point O_1 at the open end of the FS rotates clockwise by angle γ, and the closed-end rotates clockwise by angle α. The WG forces the neutral curve of the FS to undergo elliptical deformation, so that

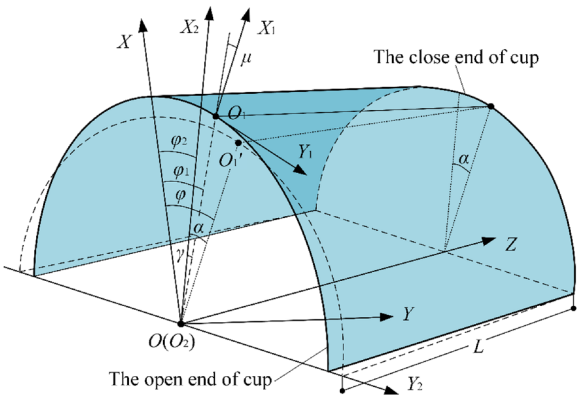

Figure 1 Coordinate systems of harmonic drive

the position of O_1 point moves from O_1' to O_1 in Figure 1, and the normal direction changes from OO_1' to X_1 axis. After the WG is installed in the FS cylinder, the FS neutral curve in different sections normal to the rotating axis has different maximum radial displacements. $a(z)$ is the semi-length of the major axis of the neutral curve in each section of the FS, which can be expressed as a function of z.

$$a(z) = r_m + d_a(z), \tag{1}$$

where r_m is the radius of the FS neutral surface before deformation, $d_a(z)$ is the function of the maximum radial displacement of the FS, which will be obtained by finite element analysis of the FS assembly deformation in Section 3.1.

The semi-length of the minor axis $b(z)$ can be determined according to the assumption (4).

$$b(z) = \tfrac{1}{9}\left\{(12r_m - 7a(z)) + \left(4\sqrt{a(z)(3r_m - 2a(z))}\right)\right\}. \tag{2}$$

To facilitate elliptic integration, all kinematic parameters are expressed as a function of ϕ_1. ϕ_1 is the angle that designates the clockwise rotation of point O_1, located at the open end of the FS, relative to the X axis. According to the parametric equation of the standard ellipse, the polar radius of the neutral curve in each section can be expressed in polar coordinates as

$$r(\varphi_1) = r = \frac{a(z)b(z)}{\sqrt{a(z)^2\sin^2\varphi_1 + b(z)^2\cos^2\varphi_1}}, \tag{3}$$

where r is the polar radius of OO_1.

According to Ref. [11], the equations of the kinematic parameters and their derivatives in Figure 1 can be derived as follows.

$$\frac{\mathrm{d}r}{\mathrm{d}\varphi_1} = \dot{r} = -\frac{a(z)\varepsilon^2\sin\varphi_1\cos\varphi_1}{\left(1+\varepsilon^2\sin^2\varphi_1\right)^{\frac{3}{2}}}, \tag{4}$$

$$\varphi = \frac{1}{r_m}\int_0^{\varphi_1}\sqrt{r^2+\dot{r}^2}\mathrm{d}\varphi_1, \tag{5}$$

$$\varphi_2 = \frac{Z_1}{Z_2 r_m}\int_0^{\varphi_1}\sqrt{r^2+\dot{r}^2}\mathrm{d}\varphi_1, \tag{6}$$

$$\mu = \arctan\frac{-\dot{r}}{r} = \arctan\frac{\varepsilon^2\sin\varphi_1\cos\varphi_1}{1+\varepsilon^2\sin^2\varphi_1}, \tag{7}$$

$$\gamma = \varphi_1 - \varphi_2, \tag{8}$$

$$\beta = \gamma + \mu, \tag{9}$$

where μ is the angle between the polar radius OO_1 and the X_1 axis. ε is the second eccentricity of the ellipse, $\varepsilon = \sqrt{a(z)^2 - b(z)^2}/b(z)$.

The coordinate system S_2 shown in Figure 1 can be converted to S_1, the coordinate transfer matrix $\boldsymbol{M_{12}}$ and the base vector transfer matrix $\boldsymbol{W_{12}}$ can be expressed as follows.

$$\boldsymbol{M_{12}} = \begin{bmatrix} \cos\beta & \sin\beta & -r\cos\mu \\ -\sin\beta & \cos\beta & r\sin\mu \\ 0 & 0 & 1 \end{bmatrix}, \tag{10}$$

$$\boldsymbol{W_{12}} = \begin{bmatrix} \cos\beta & \sin\beta & 0 \\ -\sin\beta & \cos\beta & 0 \\ 0 & 0 & 1 \end{bmatrix}. \tag{11}$$

According to the conjugate theory, the normal vector of the tooth surface and the relative velocity at the meshing contact point are perpendicular to each other. That is to say, the conjugation condition can be expressed as follows [11].

$$\boldsymbol{n_i} \cdot \boldsymbol{v_i^{(12)}} = 0 (i = 0, 1, 2), \tag{12}$$

where $\boldsymbol{n_i}$ is the normal vector of the contact point of two conjugate surfaces, and the subscript i represents the coordinate system S_i. $\boldsymbol{v_i^{(12)}}$ is the relative velocity vector of the contact point.

In the coordinate system S_1, substituting $\boldsymbol{n_1} = \boldsymbol{W_{12}}\boldsymbol{n_2}$ and $\boldsymbol{v_1^{(12)}} = \frac{\mathrm{d}\boldsymbol{r_1}}{\mathrm{d}t} = \frac{\mathrm{d}\boldsymbol{M_{12}}}{\mathrm{d}t}\boldsymbol{r_2}$ into Eq. (12), it can be transformed into

$$\boldsymbol{n_1} \cdot \boldsymbol{v_1^{(12)}} = \boldsymbol{n_2^{\mathrm{T}}}\boldsymbol{W_{12}^{\mathrm{T}}}\frac{\mathrm{d}\boldsymbol{M_{12}}}{\mathrm{d}t}\boldsymbol{r_2} = 0, \tag{13}$$

$$\boldsymbol{n_2^{\mathrm{T}}}\Phi\frac{\mathrm{d}\varphi_1}{\mathrm{d}\varphi}\frac{\mathrm{d}\varphi}{\mathrm{d}t}\boldsymbol{r_2} = \boldsymbol{n_2^{\mathrm{T}}}\Phi\boldsymbol{r_2}\frac{\mathrm{d}\varphi_1}{\mathrm{d}\varphi} = 0, \tag{14}$$

where,

$$\Phi = \boldsymbol{W_{12}^{T}}\frac{\mathrm{d}\boldsymbol{M_{12}}}{\mathrm{d}\varphi_1}. \tag{15}$$

Substituting $\frac{\mathrm{d}\boldsymbol{M_{12}}}{\mathrm{d}\varphi_1} = \begin{bmatrix} -\dot{\beta}\sin\beta & -\dot{\beta}\cos\beta & r\dot{\mu}\cos\mu + \dot{r}\sin\mu \\ \dot{\beta}\cos\beta & -\dot{\beta}\sin\beta & r\dot{\mu}\sin\mu - \dot{r}\cos\mu \\ 0 & 0 & 0 \end{bmatrix}$ and $\boldsymbol{W_{12}^{\mathrm{T}}} = \begin{bmatrix} \cos\beta & \sin\beta & 0 \\ -\sin\beta & \cos\beta & 0 \\ 0 & 0 & 1 \end{bmatrix}$ into Eq. (15), then the following matrix can be obtained

$$\Phi = \begin{bmatrix} 0 & -\dot{\beta} & \dot{\beta}r\cos\gamma - \dot{r}\sin\gamma - \dot{\gamma}r\cos\gamma \\ \dot{\beta} & 0 & -\dot{\beta}r\sin\gamma - \dot{r}\cos\gamma + \dot{\gamma}r\sin\gamma \\ 0 & 0 & 0 \end{bmatrix}. \tag{16}$$

In the cross-section where the Z coordinate value is z_i, the kinematic parameters and their derivatives are obtained according to Eqs. (1)–(9) and the maximum radial displacement function $d_a(z)$. The CS tooth profile curve $\widetilde{C}$ is expressed as a function of arc length s. For

Table 1 Design parameters of harmonic gear

Parameter	Value	Parameter	Value
Transmission ratio i	50	Modulus m (mm)	0.5
Tooth number of FS Z_1	100	Rated torque T (Nm)	33
Tooth number of CS Z_2	102	Radial deformation coefficient d_{a0}^*	0.88

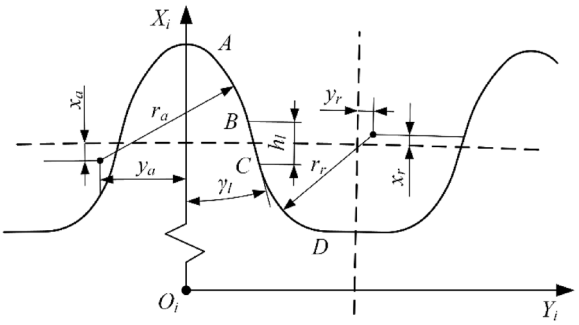

Figure 2 The schematic diagram of double-circular-arc tooth profile with common-tangent

each point on the tooth profile curve $\widetilde{C}$, there is a parameter value $s_j(j = 1, 2,..., s)$. The vectors $\boldsymbol{r_2}$ and $\boldsymbol{n_2}$ of each point are substituted into Eq. (13) to obtain the angle ϕ_1 when this point performs conjugate motion, which is recorded as $\phi_{1j}(j = 1, 2, ..., s)$. Substituting ϕ_{1j} into Eq. (17), the theoretical tooth profile curve $\widetilde{F}$ of the FS conjugated with the CS tooth profile curve $\widetilde{C}$ can be obtained.

$$\boldsymbol{r_i^{(1)}} = \boldsymbol{M_{12}} \cdot \boldsymbol{r_i^{(2)}} (i = 0, 1, 2). \tag{17}$$

3 Solution of Three-Dimensional Conjugate Tooth Surface Design

To thoroughly analyze the detailed elastic coning deformation of the FS, the finite element method is employed to study how the FS deforms when subjected to the influence of the WG. The design parameters of HD are shown in Table 1. Figure 2 shows the double-circular-arc tooth profile with common-tangent, and Table 2 shows the specific tooth profile parameters.

3.1 Analysis of the Coning Deformation of Flexspline

Figure 3 shows the finite element model of the FS coning deformation considering the specific structure of the flexible bearing.

The model is jointly developed by HyperMesh and Abaqus. All components are considered flexible bodies. The mesh of each component will be shown in detail in Section 5. The end face of the FS flange and

Table 2 Tooth profile parameters of HD

	Parameter	FS	CS
AB arc	X axis offset x_a (mm)	0.1630	0.2489
	Y axis offset y_a (mm)	−0.3450	0.4463
	Radius r_a (mm)	0.6342	0.74
BC arc	Longitudinal length h_l (mm)	0.2456	0.26
	Obliquity angle γ_l (°)	29.6715	30
CD arc	X axis offset x_r (mm)	0.1303	−0.0236
	Y axis offset y_r (mm)	−0.0249	−0.1745
	Radius r_r (mm)	0.5011	0.31

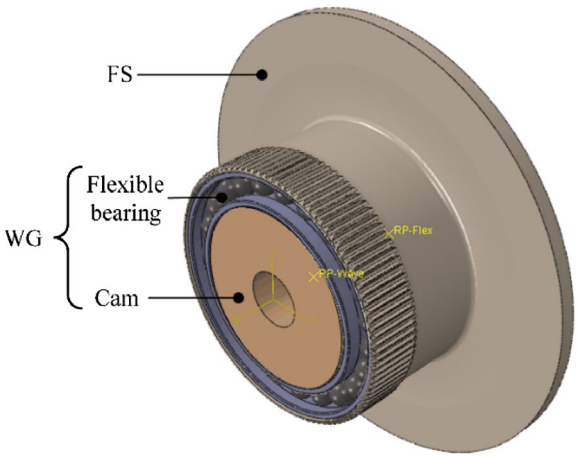

Figure 3 Finite element model of flexspline coning deformation

Table 3 Material mechanics properties of parts of HD

Parameter	Material	Young's modulus E (GPa)	Poisson's ratio v
FS	30CrMnNi	196	0.3
CS	QT400	130	0.27
WG	GCr15	208	0.3

the inner hole of the WG cam constrain all degrees of freedom. The tie constraint between the inner race and the rollers of the flexible bearing ensures the positions of the rollers and avoids rigid body displacement [17]. All other contact pairs adopt surface-to-surface contact. The friction coefficient between the rollers and the outer race is 0.02 [3], and that of the remaining contact pairs is 0.15 [18]. The material properties are shown in Table 3. The elliptical cam and the inner race have an interference fit. The cam automatically adjusts the initial interference to cause the deformation of the flexible bearing and the FS. This will enable the simulation of the flexspline assembly. Figure 4 shows the assembly

displacement distribution of the FS. The open end of the FS has the largest radial displacement, and the close-end has almost no deformation, which shows as a coning deformation. The FS teeth have an outward inclination angle θ_1 at the major axis, and an inward inclination angle θ_2 at the minor axis. In this paper, the cross-section where the WG is located is defined as the main section (design section).

To extract the detailed data of the FS coning deformation, 41 circular paths are established on the FS neutral surface. The circular path is evenly distributed along the rotating axis. As shown in Figure 5, the 0° polar axis is at the minor axis of the WG, and the counterclockwise direction is positive.

Figures 6, 7 and 8 show the radial deformation, tangential deformation and axial deformation distribution of the opening part on the FS neutral surface. The distribution of these three types of deformation exhibits a distinct periodic pattern, with both positive and negative values. The radial deformation has obvious conical characteristics along the rotating axis, tilting outward at the major axis and tilting inward at the minor axis. The maximum and minimum values are 0.511 mm and − 0.501 mm, respectively. The tangential deformation value has a conical characteristic along the rotating axis. The absolute value between the major axis and the minor axis is relatively large, and the value at the major and minor axis is close to zero. The maximum and minimum values are 0.258 mm and − 0.255 mm, respectively. Taking the

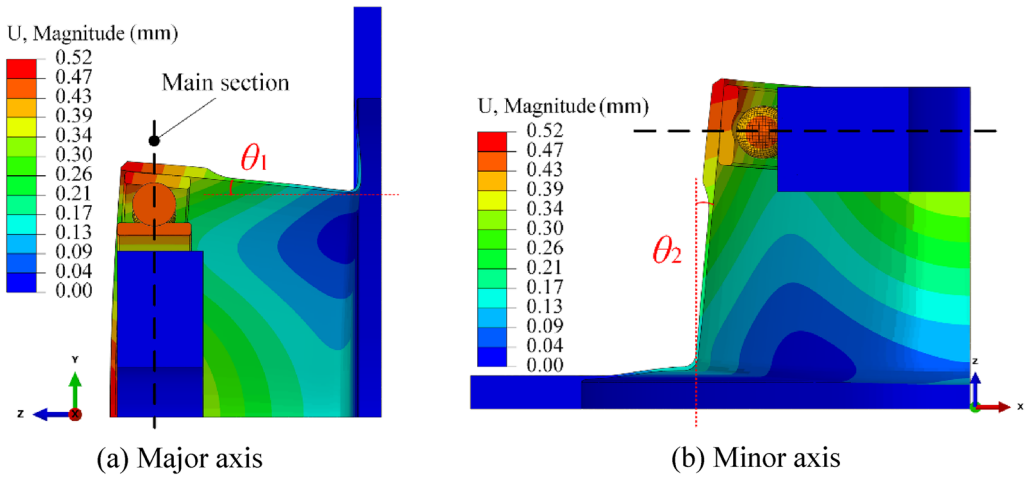

Figure 4 The assembly deformation of flexspline cylinder

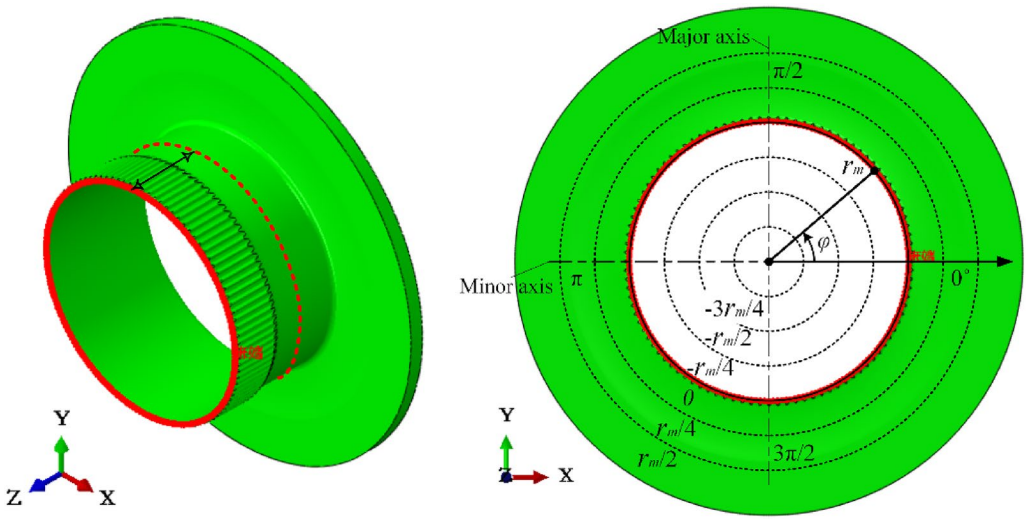

Figure 5 Circular path on flexspline neutral surface

Z-axis direction in Figure 5 as positive, the highest value of axial deformation is 0.146 mm at the minor axis, and the minimum value is − 0.101 mm at the major axis. The conical characteristic is not obvious. Among the three deformations, the radial deformation has the largest value, the tangential deformation is the second, and the axial deformation is the smallest. All have obvious conical characteristics except for the axial deformation.

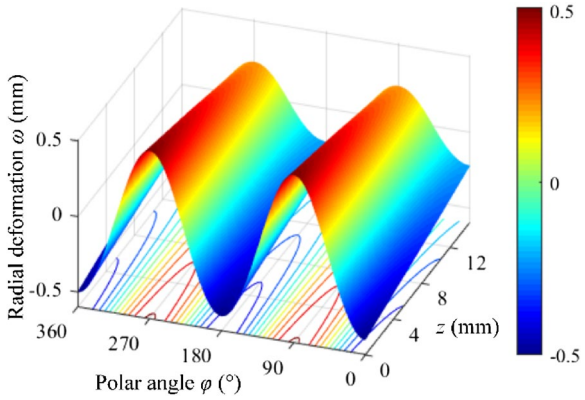

Figure 6 The radial deformation

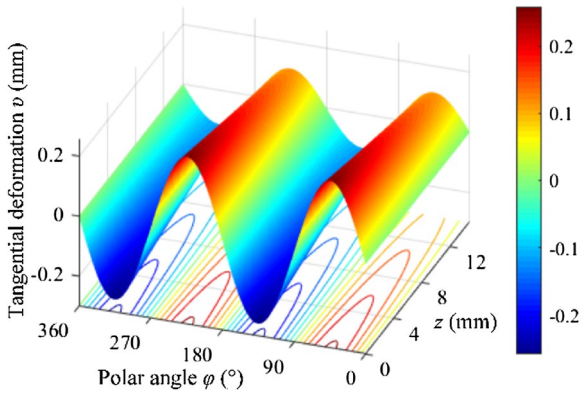

Figure 7 The tangential deformation

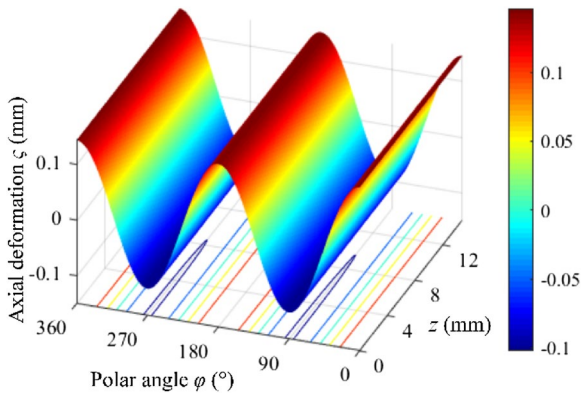

Figure 8 The axial deformation

The axial deformation of the FS neutral surface is relatively small compared to the radial and tangential deformation. This only affects the stress distribution of the shell, but does not affect the kinematics of the harmonic drive [1]. Therefore, the axial deformation is ignored. Based on the extracted detailed data of the neutral surface deformation, the method in Ref. [19] is used to perform ellipse fitting on the neutral curve data of each cross-section. Based on the result of the ellipse fitting, the maximum radial displacement in each cross-section of the FS neutral surface is represented by the blue data points in Figure 9(a). The maximum radial displacement is basically linear with the Z coordinate. The farther from the open end of the FS cup, the smaller the displacement, which is consistent with the experimental results in Ref. [1]. A linear regression analysis is conducted on the data representing the largest radial displacement. The resulting fitted straight line and the corresponding fitting error are displayed in Figure 9(a) and (b) respectively.

The maximum radial displacement function of the FS neutral surface obtained by straight-line fitting is as follows.

$$d_a(z) = kz + c, \tag{18}$$

where z is the axial coordinate value of each section, $k = 0.0185953$, $c = 0.5102824$.

3.2 Analysis of the Conjugate Existent Domain and Conjugate Tooth Profile

Currently, the primary methods used for processing the CS involve gear shaping and wire-cut electrical discharge machining. Manufacturing complex 3D tooth surfaces on the CS is challenging and not cost-effective. As a result, the CS tooth is designed as a spur gear, while the FS tooth is designed as a spatial tooth surface that is conjugated with the CS tooth surface. In the coordinate system S_2, the FS gear part is equally divided into 41 sections along the rotating axis, and the cross-sections from the 1st to the 41st correspond to $z = 0, 0.3, 0.6, ..., 12$, respectively. The main section corresponds to $z = 4$ mm.

Figures 10(a) and (b) are the axonometric view and the front view of the conjugate existent domain (CED), respectively. The bold dashed line indicates the two CEDs in the main section, and the solid line represents the CED of all other sections. The red/black one is 1st CED, and the green/ blue one is 2nd CED. The angle range of the 1st CED in the main section is [−1.245°, 7.34°], and that of the 2nd CED is [41.995°, 91.834°]. The angle ranges covered by the 1st and 2nd CED in all sections are [−1.245°, 29.931°] and [23.931°, 91.834°], respectively. The

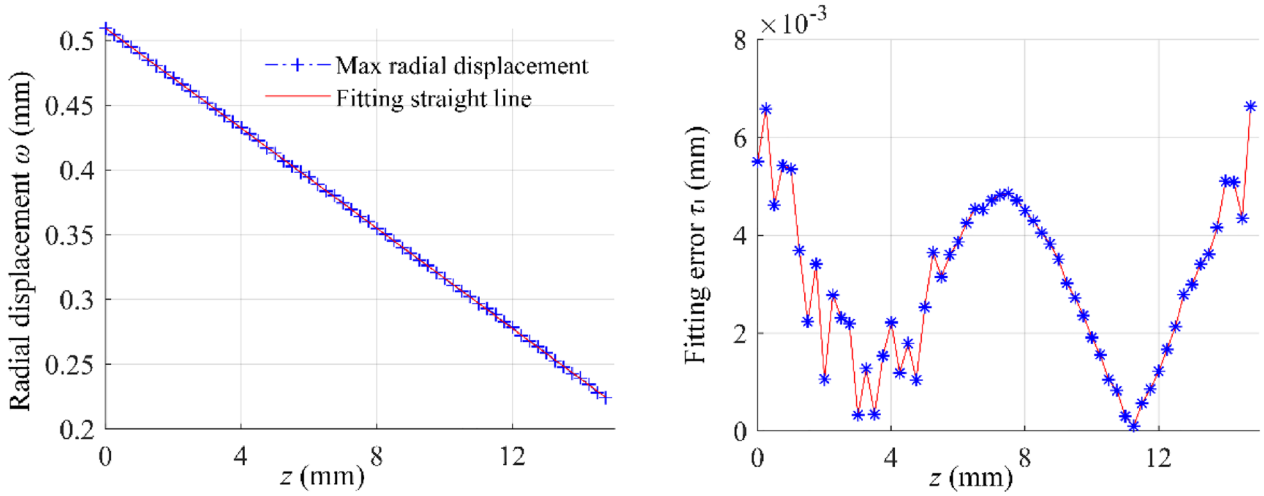

(a) Straight-line fitting of max radial displacement

(b) Fitting error

Figure 9 Straight-line fitting and fitting error of maximum radial displacement

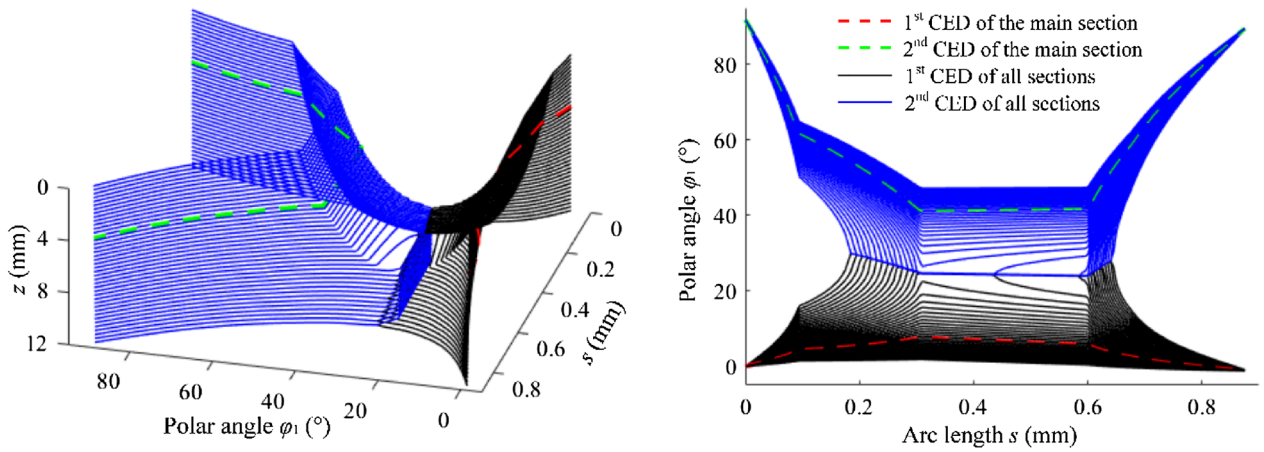

(a) Axonometric view

(b) Front view

Figure 10 Conjugate existent domain of the CS with spur gear tooth surface

expansion of the maximum angle range of the 1st and 2nd CED of the entire FS is 263.1% and 36.245% of the main section, respectively. The above analysis shows that the 1st CED of the entire FS gear part is 3.631 times the main section, which significantly increases the 1st CED. Increasing the number of gear teeth engaged in meshing is crucial for enhancing the transmission precision and torsional stiffness of HD. Substituting the CED into Eq. (17), the initial tooth surface of the FS conjugated to the CS tooth profile can be obtained. Since there are two CEDs, each section has two FS tooth profiles, as shown in Figure 11.

The bold dashed line indicates the FS tooth profile in the main section, the red one is the 1st conjugate tooth profile (CTP), and the green one is the 2nd CTP. The two tooth profiles in the main section are positioned apart from each other and do not intersect, but only one of them is viable. Solid lines represent the CTP of all other sections, black lines represent the 1st CTP, and blue lines represent the 2nd CTP. The line type and color correspond to the CED in Figure 10. Due to the coning

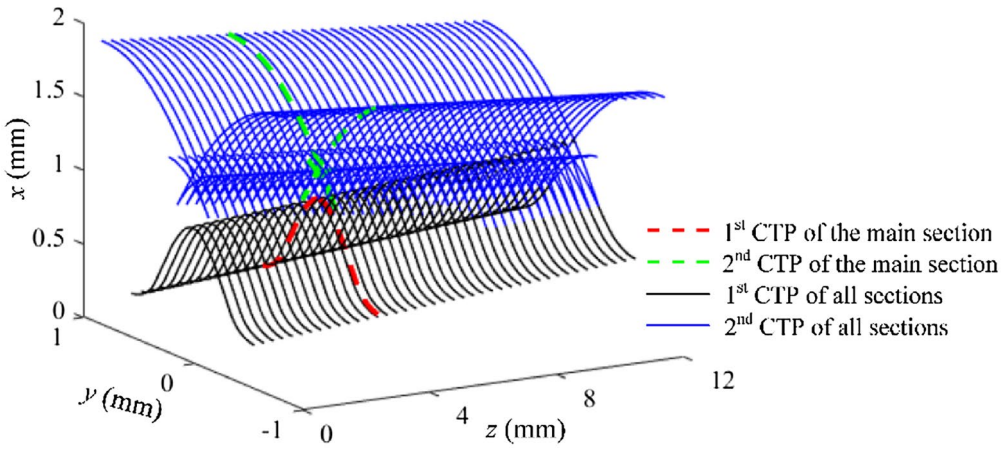

Figure 11 Initial tooth surface of the flexspline

deformation of the FS, CEDs overlap in a portion of the section, as shown in Figures 10 and 11. To analyze the overlapping phenomenon in detail, the movement trail of the CS tooth space relative to the tooth profile of the FS is calculated based on the kinematics model of HD in Section 2. It must be noted that the FS tooth profile in all 41 sections will form a 3D FS tooth surface. This will ensure the accuracy of the desired tooth surface. As a result of a large number of cross-sections, the results of 4 typical cross-sections will be explained in detail. The Z coordinates of the 4 typical cross-sections in the coordinate system S_2 are $z = 0$, 4, 8, and 12.

Figures 12, 13, 14 and 15 display front views of CED and CTP in four representative cross-sections, as illustrated in subpanels (a) and (b). Among them: 1 tip transition arc (green), 2 addendum circular arc (blue), 3 common-tangent segment (black), 4 dedendum circular arc (red), 5 root transition arc (sky blue). Figures 12, 13, 14 and 15 illustrate that with an increase in the Z coordinate, the radial displacement of the FS neutral curve decreases. Consequently, this leads to the gradual convergence and eventual overlap of the two CEDs and two CTPs. When two CEDs overlap in a certain cross-section, the two CTPs in the same section will also overlap. The overlap of the CED starts from the common-tangent segment and extends to the addendum circular arc and the dedendum circular arc. Finally, the overlapping arc length of the CED accounts for 51% of the total arc length, which is more than half. The solved 1st and 2nd CTPs of the FS are formed by the envelope of CS tooth space at different positions. The CED of the 1st CTP is near 0°. At this position, the tooth pairs of the CS and the FS are in full engagement. The CED of the 2nd CTP is distributed in a wide range around ± 90°. At this position, the tooth pairs of the CS and the FS are in the engage-in or engage-out state.

3.3 Optimization of the Overlapping Conjugate Tooth Profile

Figures 12, 13, 14 and 15 demonstrate that as the Z coordinate increases, the 1st and 2nd CTPs initially diverge, followed by a gradual convergence, and eventually overlap. This phenomenon introduces uncertain factors in determining the available CTP, adding complexity to the process. When the two CTPs do not overlap or intersect, the 1st CTP is considered the available CTP, as shown in Figures 12 and 13. However, when the two CTPs are overlapping and intersecting, if the 1st CTP is used as the available CTP, it will cause significant meshing interference, as shown in Figures 14 and 15. In such a section, a part of the 2nd CTP appears inside the 1st CTP. The available CTP should be composed of the 1st and 2nd CTPs, as shown in Figures 16 and 17.

When comparing Figures 14 and 15 with Figures 16 and 17, and specifically focusing on the cross-section where the two CEDs overlap, it can be observed that the 1st and 2nd CTPs of the CS tooth profile segment, after the point of overlap, collectively form the available CTP. In other words, the available CTP of the FS in this cross-section is formed by the envelope of the CS tooth tip. In the cross-section where the two CTPs overlap and intersect, the method shown in Figures 16 and 17 is used to determine the available tooth profile in this section to eliminate unnecessary meshing interference. Due to a large number of cross-sections, Matlab code was written to calculate the available tooth profile in each section. Figure 18 shows the available FS tooth surface calculated by Matlab code, and the specific calculation process is as follows:

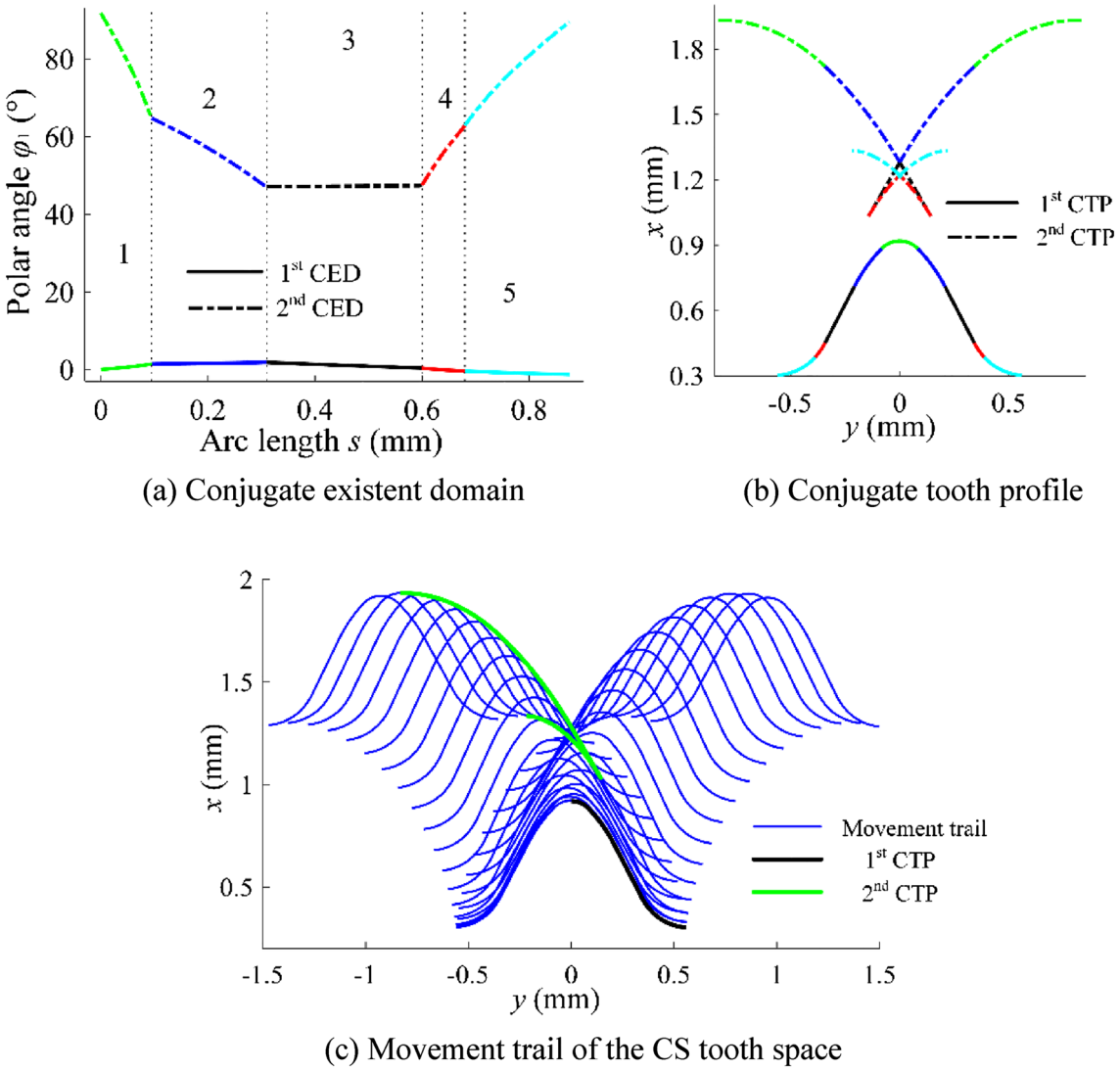

Figure 12 The enveloping process of flexspline tooth profile at $z = 0$ mm

(1) On a certain cross-section, subtract the value of the 2nd CED from that of the 1st CED.
(2) Determine whether the two CEDs overlap, if the result is NO, the 1st CTP is used as the available tooth profile, if the result is YES, move to the next step.
(3) Find the endpoint of the overlapping part, and the CTP determined jointly by the 1st and 2nd CEDs after the overlap endpoint is used as the available tooth profile.

Currently, the FS teeth in HD are mainly produced by gear hobbing. The available tooth surface of FS, as depicted in Figure 18, exhibits intricate geometric characteristics, with variations in the tooth profile along the axial direction in each section. This makes the manufacture of the tooth surface very difficult. As a result, considering both economy and feasibility, the machinable tooth surface is obtained by applying the tooth profile in the main section to all sections and then reasonably adjusting its position along the radius. The machinable tooth surface design aims to preserve the geometric characteristics of the available tooth surface to the greatest extent possible.

In all sections, the reasonable adjustment of the radial position satisfies the following 2 constraints:

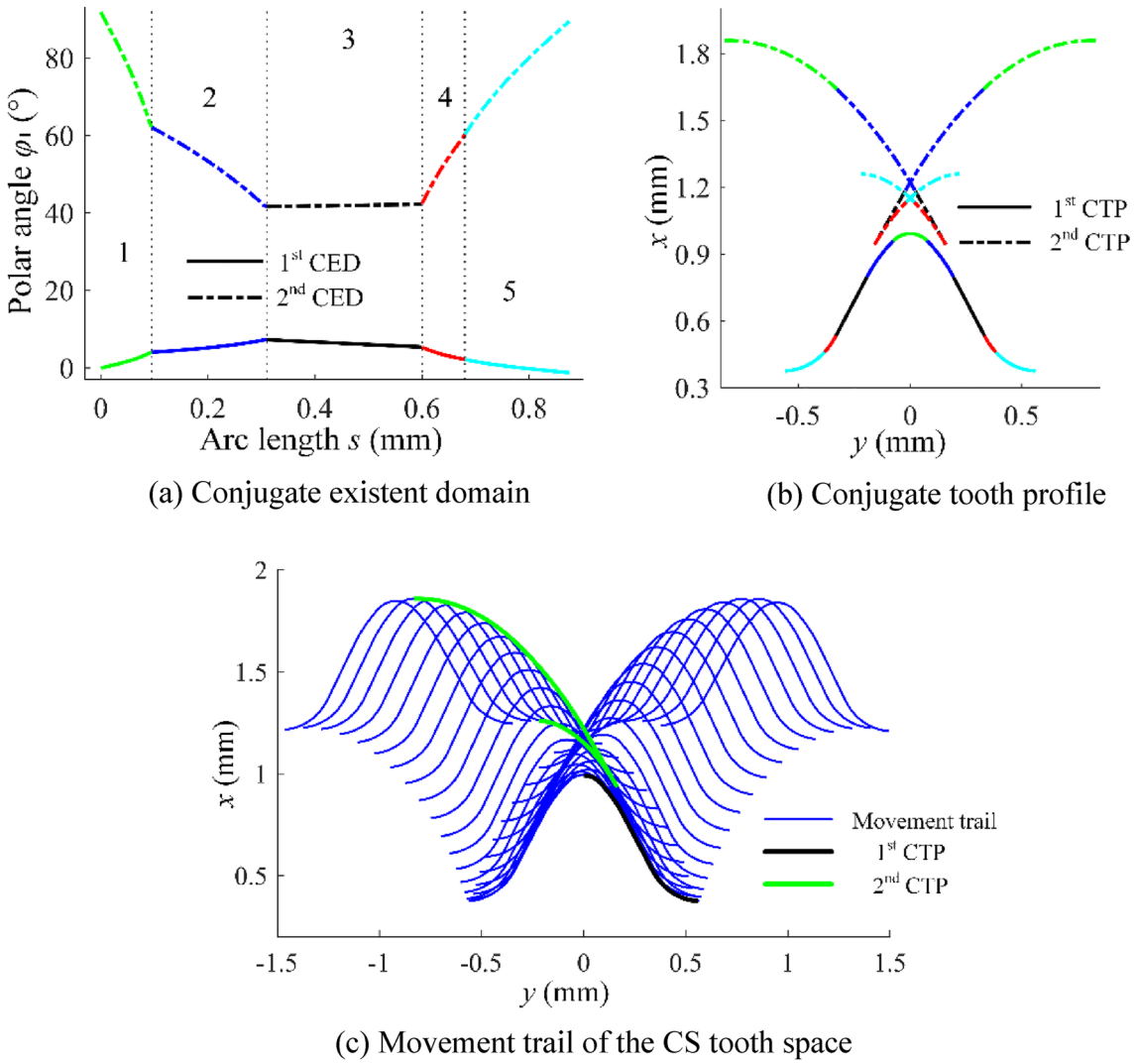

Figure 13 The enveloping process of flexspline tooth profile at $z = 4$ mm

(1) To avoid the meshing interference of the gear pairs of the FS and the CS, it is necessary to ensure that the machinable tooth profile is located inside the available tooth surface area.
(2) To retain the geometric features of the available tooth surface as much as possible, it must be ensured that part of the machinable tooth profile coincides with the available tooth surface.

The available tooth profile coordinates in each section minus the coordinates of the tooth profile in the main section, to obtain the radial movement Δh that satisfies the above two constraints. Figure 19 shows that $\widetilde{U}$ is the available tooth profile in any section, $\widetilde{M}$ is the tooth profile in the main section, and the coordinates of a point on $\widetilde{U}$ and $\widetilde{M}$ are (x_u, y_u, z_u) and (x_m, y_m, z_m), respectively. In any section, $z_u = z_m$ is satisfied, when $y_{uj} = y_{mj}$, $\Delta x_j = x_{uj} - x_{mj}$, then $\min(\Delta x_j)$ $(j = 1, 2, \ldots, s)$ is taken as the radial displacement Δh in this section. Figure 20 shows the calculation results of the radial displacement Δh in all sections. Figure 21 illustrates that the tooth profile in every cross-section of the machinable tooth surface remains consistent, enabling direct manufacturing through gear hobbing. Additionally, Figure 22 demonstrates the iterative calculation process for optimizing the overlapping conjugate tooth profile.

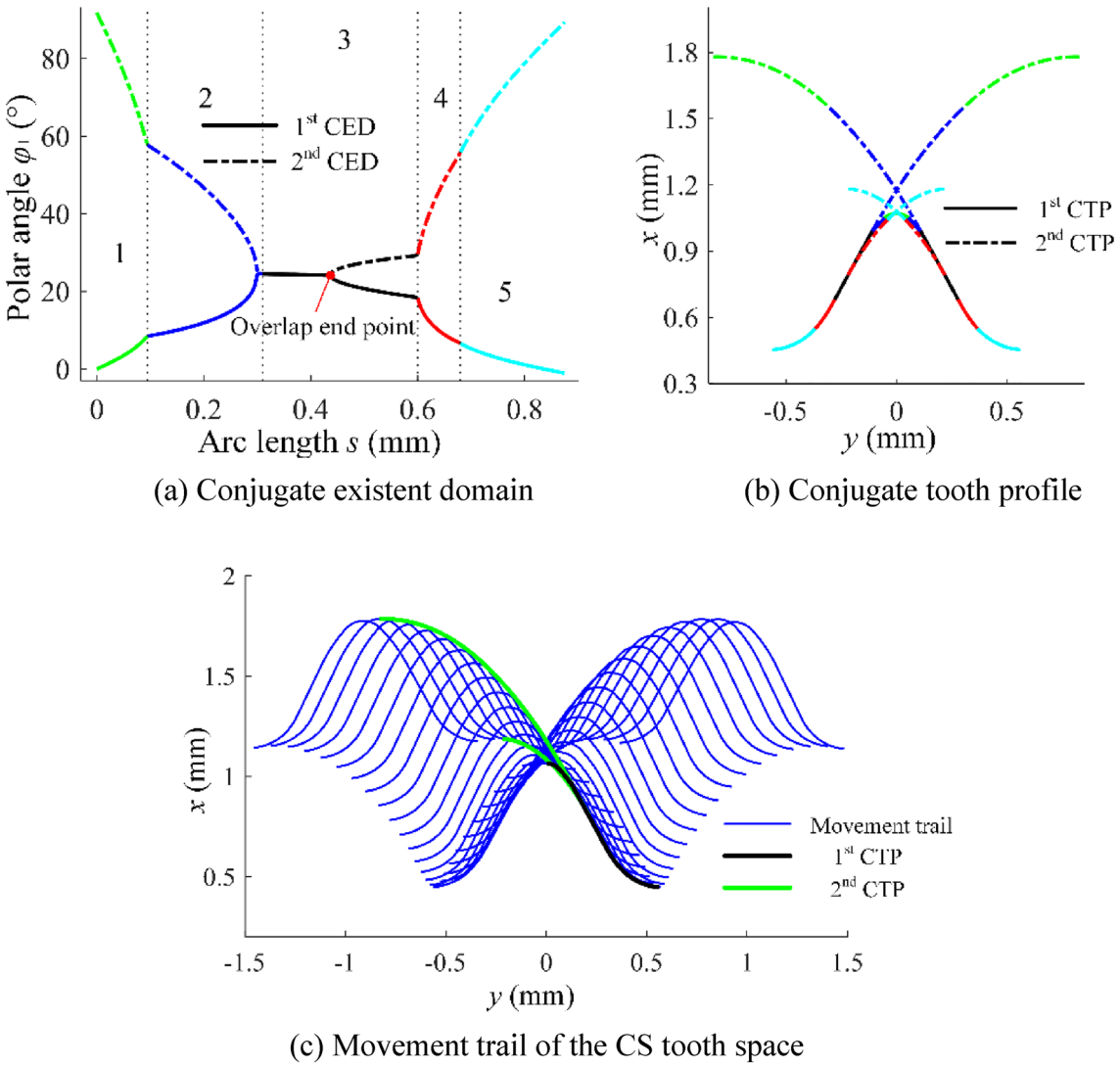

Figure 14 The enveloping process of flexspline tooth profile at $z = 8$ mm

3.4 Modeling of the FS with Machinable Tooth Surface

Due to the varying radial displacements across each cross-section of the machinable tooth surface, establishing a precise 3D model solely within CAD software presents challenges. The author combined Matlab and Solidworks to create an accurate 3D model of the FS with the machinable tooth surface. The main steps are as follows:

(1) Use the Curve Fitting Tool in Matlab to fit the radial displacement data in all sections of the machinable tooth surface, as shown in Figure 23. To ensure the accuracy of the fitting, the 8th-degree polynomial fitting is used, and the curve fitting expression is as follows:

$$F(z) = p_1 z^8 + p_2 z^7 + p_3 z^6 + p_4 z^5 + p_5 z^4 + p_6 z^3 + p_7 z^2 + p_8 z + p_9, \tag{19}$$

where $p_1 = -5.355 \times 10^{-8}$, $p_2 = 2.414 \times 10^{-6}$, $p_3 = -4.33 \times 10^{-5}$, $p_4 = 0.0003955$, $p_5 = -0.001963$, $p_6 = 0.005185$, $p_7 = -0.007033$, $p_8 = 0.02118$, $p_9 = -0.052$.

(2) Input Eq. (19) into Solidworks, draw the 2D tooth profile of the FS in the main section, and use the

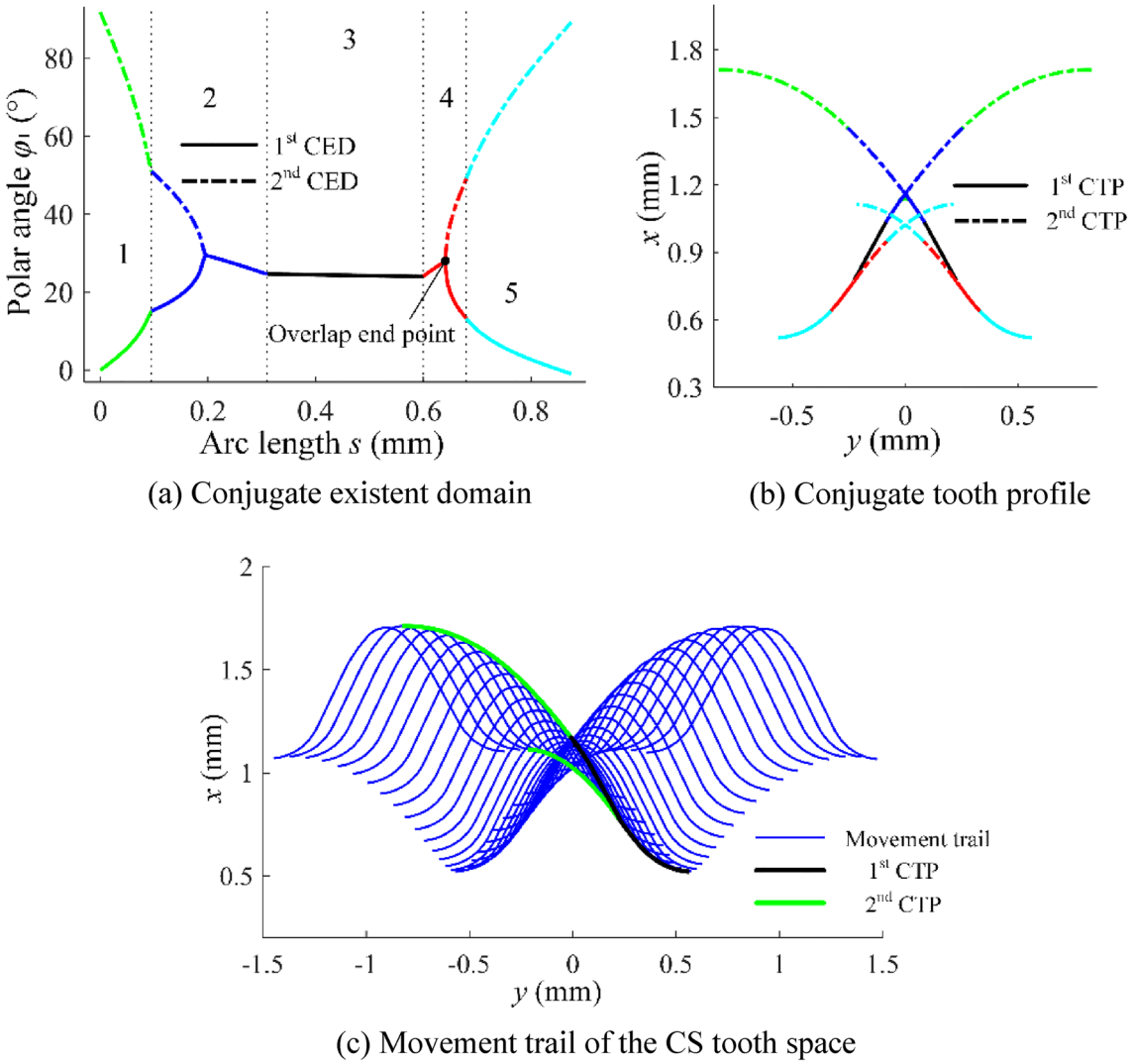

Figure 15 The enveloping process of flexspline tooth profile at $z = 12$ mm

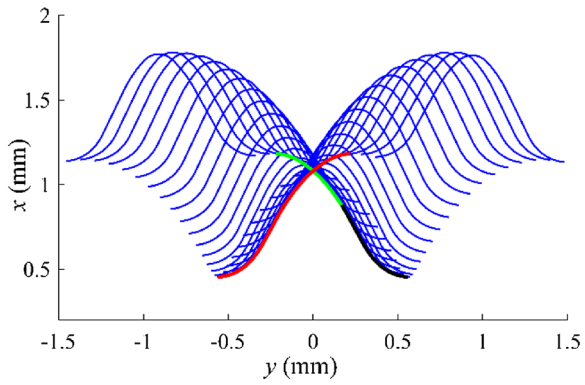

Figure 16 The available CTP at $z = 8$ mm

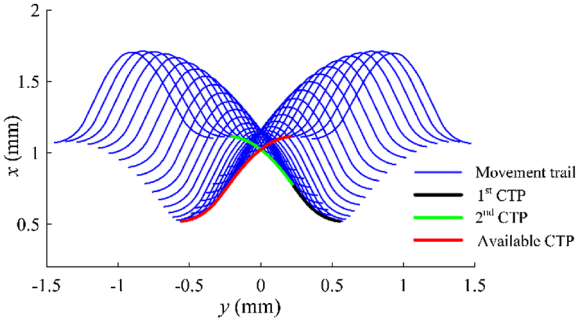

Figure 17 The available CTP at $z = 12$ mm

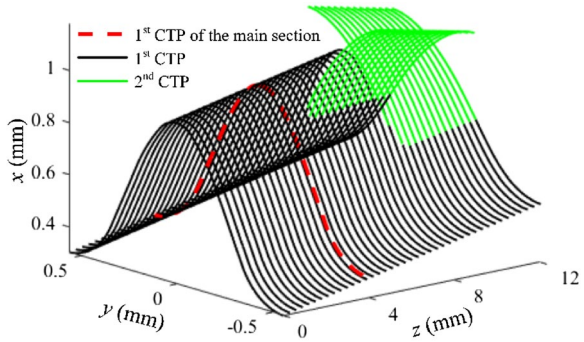

Figure 18 The available tooth surface of flexspline

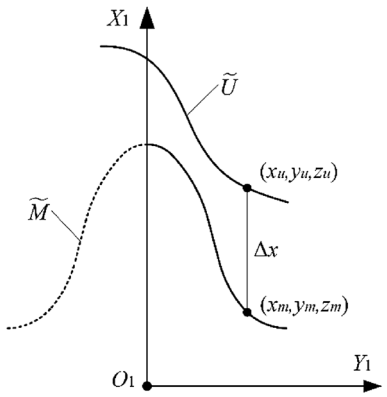

Figure 19 The radial movement Δh

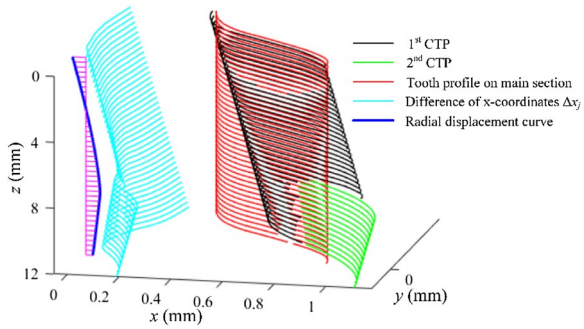

Figure 20 The schematic diagram of displacement calculation

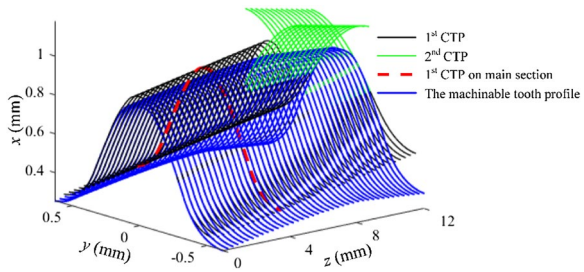

Figure 21 The machinable conjugate tooth surface of flexspline

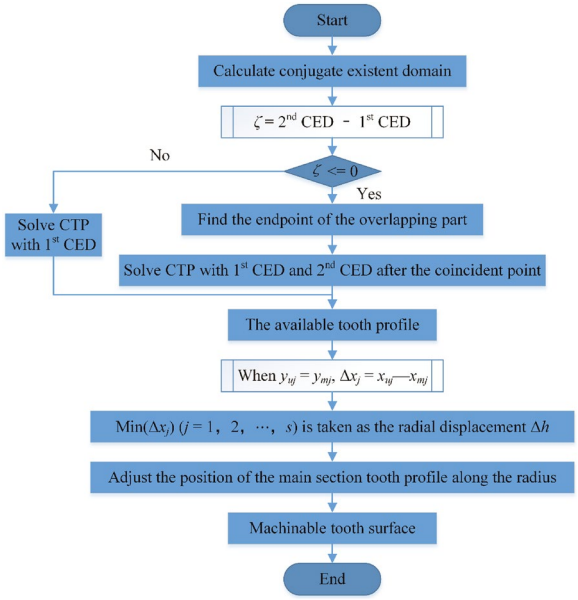

Figure 22 Calculation iterative process of overlapping conjugate tooth profile optimization

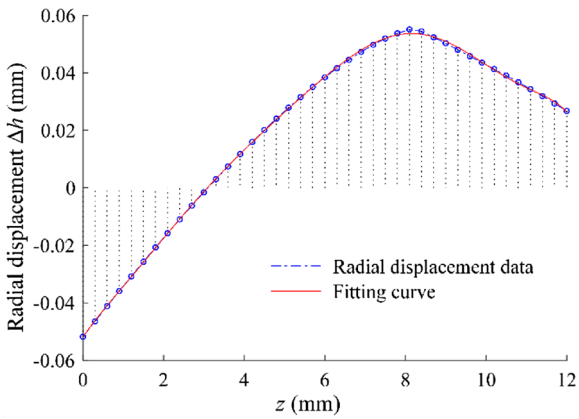

Figure 23 Radial displacement data

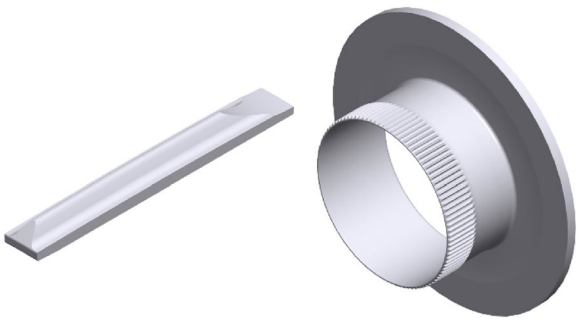

Figure 24 Three-dimensional model of the FS

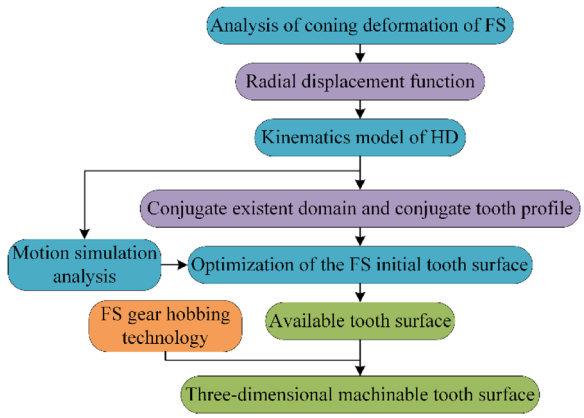

Figure 25 Frame diagram of the design method

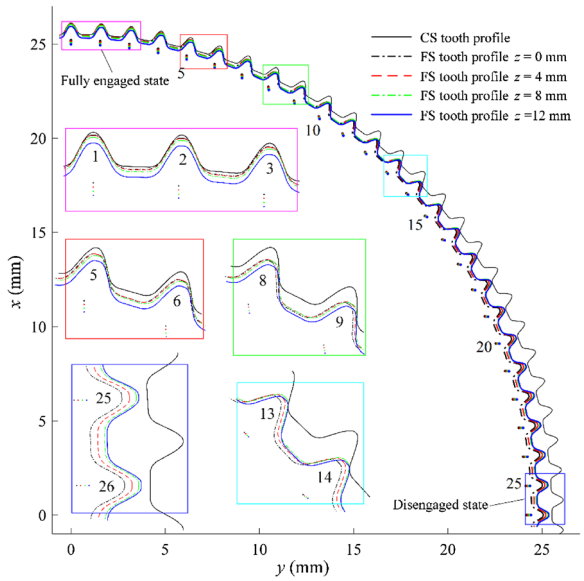

Figure 26 Assembly state diagram of machinable tooth surface

"sweep" command to draw the machinable tooth surface of the FS, as shown in Figure 24.

In summary, this paper presents a design method for the 3D tooth surface of FS. The radial deformation function of the FS, obtained through FEA, is incorporated into the kinematics model of HD. The optimization of the overlapping CTP is carried out by analyzing the tooth enveloping process of the FS. Taking into account the hobbing process of the FS, the machinable tooth surface of FS is achieved by adjusting the position of the main section tooth profile along the radial direction. The detailed process is illustrated in Figure 25.

4 Motion Simulation Analysis

To assess the rationality and superiority of the designed 3D conjugate tooth surface, a multi-section assembly and meshing motion simulation of the machinable tooth surface is conducted. Figure 26 shows the assembly simulation results in 4 typical cross-sections of the machinable tooth surface. At the major axis of the WG, teeth 1 to 3 are in full engagement, and teeth 25 to 26 at the minor axis are completely disengaged. Affected by the coning deformation of the FS, in the fully engaged state, the tooth profile in the section near the closed end ($z = 12$ mm) is at the innermost side, and the tooth profile in the open end section ($z = 0$ mm) is at the outermost side. In the disengaged state, the position of the tooth profile in the two sections is just exchanged.

Figure 27 shows the meshing motion simulation results in 4 typical cross-sections of the machinable tooth surface. The red curve represents the movement trail of the origin O_1 fixedly connected with the FS tooth. When the WG rotates 360°, the FS rotates two more teeth relative to the CS. In the process of gear tooth meshing, there is no meshing interference between CS and FS gear teeth. Part of the tooth profile in each section is always in the meshing contact state. From the open end to the closed end, the movement trail of the FS teeth gradually becomes smoother. In addition, the radial displacement is gradually reduced, which is consistent with the actual situation. In the section near the closed end, the tooth pair of the FS and the CS only engage at the top of the tooth profile. In the remaining sections, the tooth pairs of the FS and the CS maintain a continuous meshing with a significant arc length. Figure 28 shows the backlash distribution in 4 typical cross-sections of the machinable tooth surface. The abscissa represents the number of teeth. The FS tooth at the major axis of the WG is marked as 1, and the other teeth are marked as 2, 3, 4, ..., n in the clockwise direction. The ordinate represents the backlash, and if there is interference between the tooth profiles, the backlash is negative. The backlash distribution in 4 typical cross-sections is drawn with different line types. Take the backlash value of less than 0.003 mm as the possible condition for meshing contact [20], and mark the backlash value involved in the meshing with a red circle. The results indicate that there is meshing engagement between certain gear teeth in each section of the FS. The number of gear teeth participating in the meshing from the section $z = 0$ mm to the section $z = 12$ mm are 3 (1st–3rd), 5 (1st–5th), 11 (3rd–13th), and 5 (9th–14th) respectively,

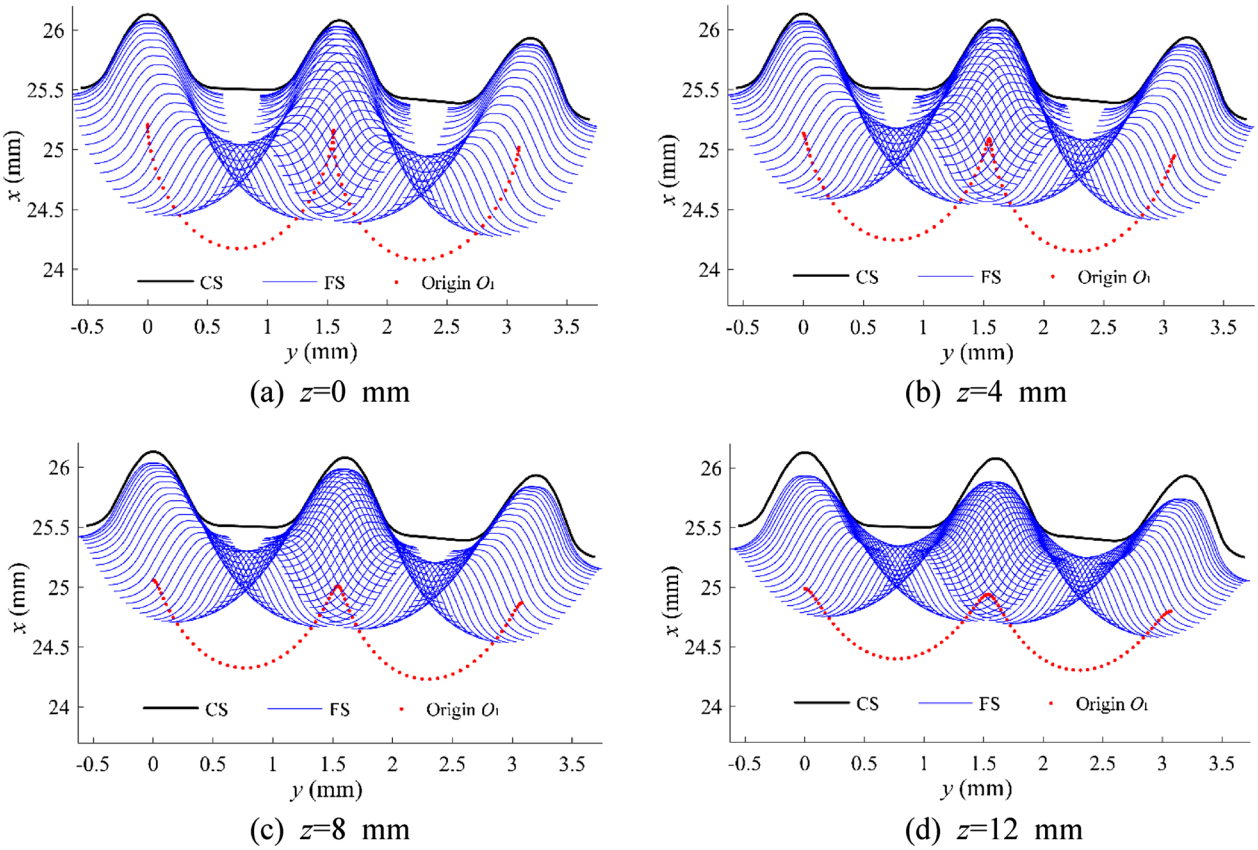

Figure 27 The relative movement trail of FS tooth profile in 4 typical cross-sections

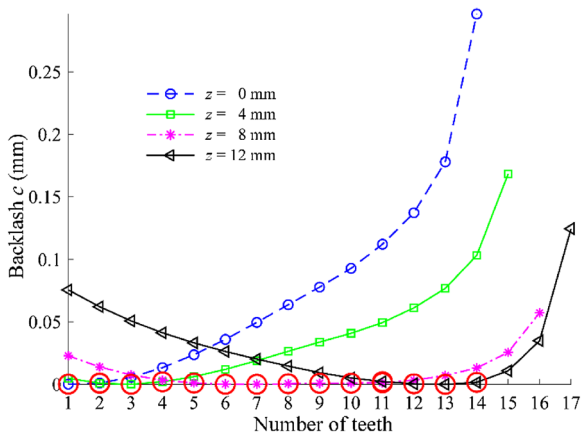

Figure 28 The distribution of minimum backlash

and the gear teeth involved in meshing gradually move away from the major axis. Although the backlash distribution varies across each section, the overall backlash distribution of the FS, comprising all sections, is notably more uniform with minimal fluctuations.

5 Loaded Tooth Contact Analysis

The finite element model of the loaded harmonic gear contact analysis is established by adding the CS component to the finite element model of the FS coning deformation in Section 3.1. All parts are divided into hexahedral element shapes, as shown in Figure 29. The material properties are shown in Table 3. Three reference points RP-Wave, RP-Flex and RP-Rigid are established, which are coupled to the inner wall of the WG cam, the end face of the FS flange and the outer wall of the CS respectively. The analysis steps are set as follows:

(1) Fix all degrees of freedom of the 3 reference points RP-i (i = Wave, Flex, Rigid), and the cam automatically adjusts the initial interference to cause the flexible bearing and the FS to deform to allow the flexspline to be assembled.
(2) A surface-to-surface contact is established between the tooth surface of the FS and CS, and the friction coefficient is 0.15.

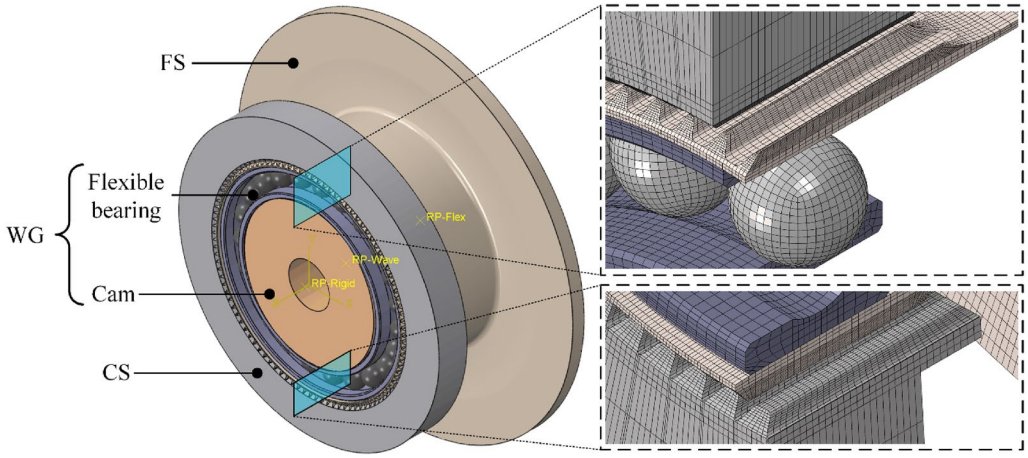

Figure 29 The finite element model of the loaded harmonic gear

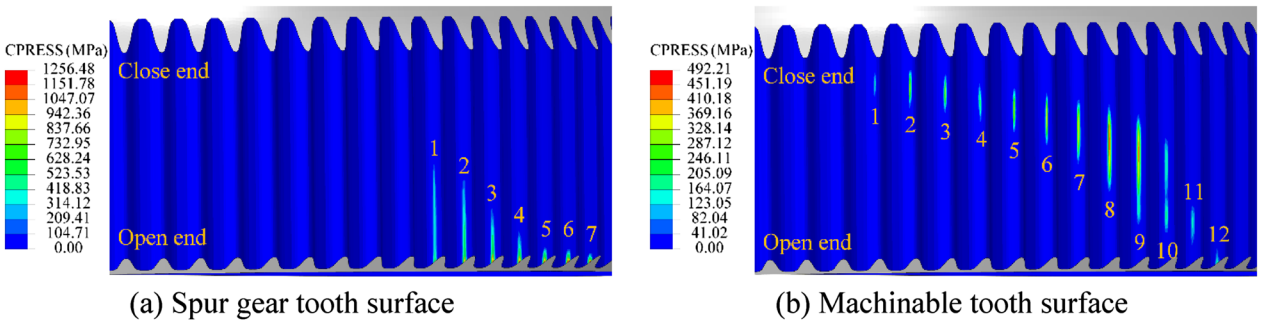

Figure 30 Contact pressure distribution in the meshing area of the FS

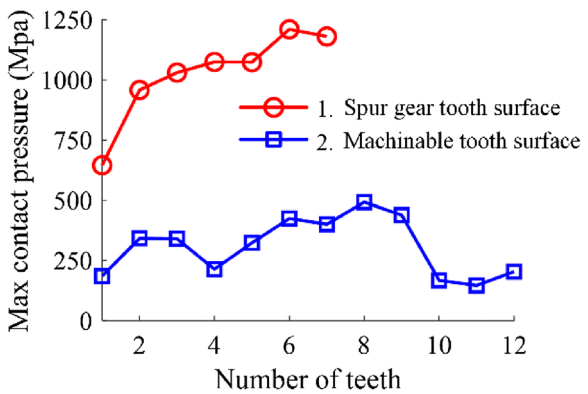

Figure 31 Maximum contact pressure distribution of the contacting gear teeth of the FS

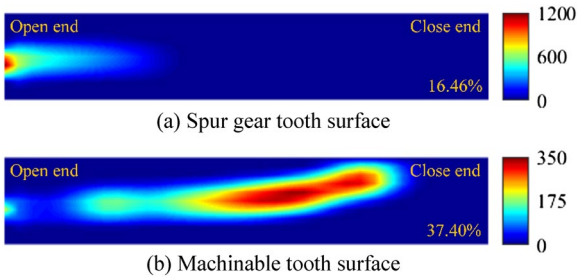

Figure 32 Contact pattern of flexspline

(3) The rotational freedom of reference point RP-Flex is released, and a counterclockwise torque of 33 Nm is applied to realize FS loading.

(4) The rotation displacement in the counterclockwise direction is applied to the reference point RP-Wave to realize the FS rotation driven by the WG.

Figure 30 shows the contact pressure distribution in the meshing area of the FS with spur gear tooth surface

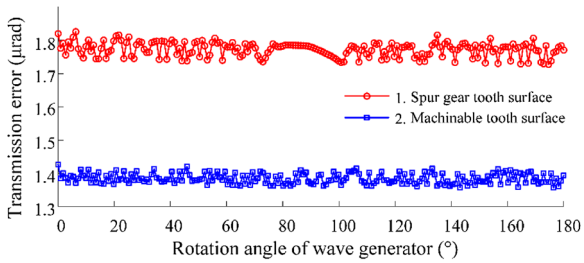

Figure 33 Transmission error

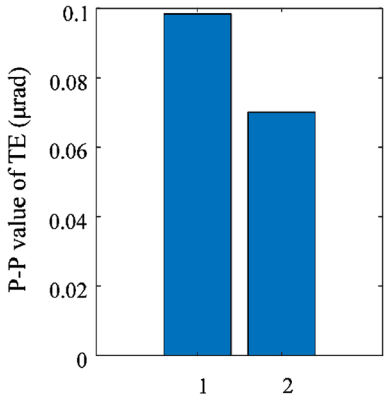

Figure 34 P-P value of TE

and the 3D machined tooth surface, respectively. In the FS with spur gear tooth surfaces, there are 7 teeth on one side and 14 on both, which accounts for 14% of the teeth. The contact patterns are mainly concentrated at the edge of the opening end, and the maximum contact pressure appears on the 6th tooth, with a value of 1256.5 MPa. The FS with the 3D machinable tooth surface has 12 teeth on one side (24 on both sides) to engage in meshing, accounting for 24%. More than 4/5 of tooth surfaces in the tooth width direction are engaged in meshing, and the meshing condition is favorable. The maximum contact pressure appears on the 8th tooth.

Figure 31 shows the maximum contact pressure distribution of the contacting gear teeth of the FS with a spur gear tooth surface and a 3D machinable tooth surface. The tooth surface of the 3D machinable gear engages with more teeth compared to the tooth surface of a spur gear, resulting in a more uniform load distribution among the teeth with reduced magnitude.

Figure 32 displays the contact pattern of FS with both a spur gear tooth surface and a 3D machinable tooth surface. In the case of FS with a spur gear tooth surface, contact occurs at the edge of the opening end. The contact pattern accounts for 16.46% of the full tooth surface, and the maximum contact pressure is 1210.14 MPa. The full tooth width direction of the FS with the 3D machinable tooth surface basically participates in meshing. The contact pattern accounts for 37.40% of the full tooth surface, which is 2.272 times that of the spur gear tooth surface. The main contact area is in the middle of the tooth width, and the maximum contact pressure (492.16 MPa) is only 40.67% of the spur gear tooth surface. Figure 33 shows the transmission error of a harmonic gear with a spur gear tooth surface and a 3D machinable tooth surface during the 180° rotation of the WG. Figure 34 shows the peak-to-peak value of transmission error (TE).

The results show that the transmission errors of the two tooth surfaces have no long-period TE. The peak-to-peak value and average value of TE of spur gear tooth surface are 0.0984 and 1.781 μrad respectively, and that of 3D machinable tooth surface are 0.0701 and 1.393 μrad respectively. The results confirm that the 3D machinable tooth surface designed in this paper exhibits its superior transmission performance compared to the tooth surface of spur gears.

6 Conclusions

This paper presents a novel method for designing a 3D conjugate tooth surface of HD with a double-circular-arc tooth profile. Additionally, an HD kinematics model is established, which considers the FS coning deformation. The designed 3D machinable tooth surface is verified through motion simulation and finite element analysis, ensuring accurate backlash distribution and loaded tooth contact characteristics. The following are the main conclusions drawn from this study:

(1) The proposed method for designing a 3D conjugate tooth surface enables the creation of an internal gear pair consisting of a spur gear tooth surface (CS) and a 3D machinable tooth surface (FS). This internal gear pair allows for multiple tooth meshings and a broader contact area on the tooth surface, enhancing its performance in HD applications.
(2) By employing multi-section assembly and motion simulation, the tooth profile in each section of the machinable tooth surface remains in constant meshing contact, ensuring that there is no interference between the CS and FS gear teeth. This results in a more uniformly distributed and minimally fluctuating overall backlash distribution in the fully assembled FS gear.
(3) Under the rated torque, 24% of the FS teeth are engaged in meshing, with over 4/5 of the tooth surface in the axial direction bearing the load. The contact patterns, maximum contact pressure,

and transmission error peak-to-peak value of the machinable tooth surface are 227.2%, 40.67%, and 71.24% of the spur gear tooth surface, respectively, demonstrating outstanding transmission performance.

Acknowledgements
Not applicable.

Author contributions
CS and FZ were in charge of the whole research; XL analyzed the transmission principle; XD was in charge of the finite element analysis. All authors read and approved the final manuscript.

Authors' Information
Chaosheng Song born in 1983, is currently a professor at *Chongqing University, China*. His main research interests include gear geometry design and tooth contact analysis.
Feihong Zhu born in 1995, is currently pursuing the Ph.D. degree in mechanical design and theory with *Chongqing University, China*. His research interests include the precision gear transmission and gear efficiency analysis.
Xinzi Li born in 1994, is currently pursuing the Ph.D. degree in mechanical design and theory with *Chongqing University, China*. His research interests include the precision gear transmission and tooth contact analysis.
Xuesong Du born in 1970, is currently an associate professor at *Chongqing University, China*. His main research interests include mechanical design and mechanical system optimization analysis.

Funding
Supported by Guangdong Provincial Key-Area Research and Development Program (Grant No. 2019B090917002).

Availability of data and materials
Not applicable.

Declarations

Competing interests
The authors declare that they have no competing interests.

Received: 5 January 2022 Revised: 8 June 2023 Accepted: 19 June 2023
Published online: 31 July 2023

References

[1] H Dong. *Study of kinematics and meshing characteristic of harmonic gear drives based on the deformation function of the flexspline*. Dalian: Dalian University of Technology, 2008. (in Chinese)
[2] Y Eloy, G Ignacio, F Alfonso. Stress analysis of strain wave gear drives with four different geometries of wave generator. *Meccanica*, 2020, 55(11): 2285–2304.
[3] X Li, C Song, Y Yang, et al. Optimal design of wave generator profile for harmonic gear drive using support function. *Mechanism and Machine Theory*, 2020, 152: 103941.
[4] H Dong, D Wang, K.-L Ting. Kinematic effect of the compliant cup in harmonic drives. *Journal of Mechanical Design*, 2011, 133(5): 051004–051001.
[5] H Xin. Design for basic rack of harmonic drive with double-circular-arc tooth profile. *China Mechanical Engineering*, 2011, 22(6): 656–662. (in Chinese)
[6] F Zhu, X Du, C Song, et al. Design and analysis of space conjugate tooth profile of harmonic drive considering deformation of flexspline cup. *Journal of Central South University (Science and Technology)*, 2020, 51(9): 2471–2479. (in Chinese)
[7] Z Yu, S Ling, X Wang, et al. Study on tooth profile design of harmonic drive with deformation model of flexspline. *Meccanica*, 2021, 56 (7): 1883–1904.
[8] G Chen, H Li, Y Liu. Double-arc harmonic gear profile design and meshing analysis for multi-section conjugation. *Advances in Mechanical Engineering*, 2019, 11(5): 1–14.
[9] Y Yang, J Li, J Wang, et al. Analysis of tooth profile modification and meshing characteristics of double arc harmonic drive. *2021 4th International Conference on Electron Device and Mechanical Engineering*, IEEE, 2021: 268–273.
[10] M Majchrak, R Kohar, S Hrcek, et al. The comparison of the amount of backlash of a harmonic gear system. *Tehnički Vjesnik*, 2021, 28(3): 771–778.
[11] Y Yang, J Wang, Q Zhou, et al. Exact solution for conjugate profiles of zero backlash harmonic drives with elliptical cam wave generators. *Journal of Central South University (Science and Technology)*, 2017, 48(12): 3231–3238. (in Chinese)
[12] W Wu, P Yu, Y Hou. New design, new process of harmonic drive with short flexspline and its experiment. *Journal of Harbin Institute of Technology*, 2014, 46(1): 40–46. (in Chinese)
[13] D Liu, J Xing, X Chen. Spatial tooth profile design and simulation analysis of harmonic drive with involute tooth profile. *Computer Integrated Manufacturing Systems*, 2015, 21(3): 709–715. (in Chinese)
[14] J Wang, X Zhou, J Li, et al. Three dimensional profile design of cup harmonic drive with double-circular-arc common-tangent tooth profile. *Journal of Zhejiang University*, 2021, 55(4): 616–713. (in Chinese)
[15] X Chen. *Arc tooth profile design and simulation research of harmonic drive based on mesh backlash assessment*. Tianjin: Tiangong University, 2012. (in Chinese)
[16] X Zeng, J Li, J Wang, et al. Design and modification of harmonic double circular arc tooth profile based on finite element method. *Journal of Zhejiang University (Engineering Science)*, 2021, 55(8): 1548–1565. (in Chinese)
[17] S Wang, G Jiang, X Mei, et al. A rapid stress calculation method for short flexspline harmonic drive. *Engineering Computations*, 2019, 36(6): 1852–1867.
[18] B S Mahanto, V Sahoo, R Maiti. Effect of cam insertion on stresses in harmonic drive in industrial robotic joints. *Procedia Computer Science*, 2018, 133: 432–439.
[19] A Fitzgibbon, M Pilu, R B Fisher. Direct least square fitting of ellipses. *IEEE Transactions on Pattern Analysis and Machine Intelligence*, 1999, 21(5): 476–480.
[20] G Jiang, S Wang, X Mei, et al. Bidirectional conjugate design method for double-circular-arc tooth profile of harmonic drives. *Journal of Xi'an Jiaotong University*, 2019, 53(8): 8–14. (in Chinese)

Submit your manuscript to a SpringerOpen journal and benefit from:

► Convenient online submission
► Rigorous peer review
► Open access: articles freely available online
► High visibility within the field
► Retaining the copyright to your article

Submit your next manuscript at ► springeropen.com